Journal of the Brazilian Society of Mechanical Sciences and Engineering (2026) 48:629
https://doi.org/10.1007/s40430-026-06569-2

TECHNICAL PAPER

Longitudinal vibrations of bi-directionally functionally graded microbars with deformable boundaries

Murat Akpınar[1] · **Büşra Uzun**[1] · **Mustafa Özgür Yaylı**[1]

Received: 19 November 2025 / Accepted: 8 May 2026
© The Author(s) 2026

Abstract
The present research focuses on the longitudinal vibration analysis of a microbar resting on an elastic foundation, incorporating deformable (spring-based) boundary conditions. The material is modeled as functionally graded in two spatial directions. The governing equation for the axial vibration of the microbar is derived using the Hamilton's principle and the Aifantis strain gradient theory, which captures small-scale effects. Using the resulting governing and force boundary equations, an eigenvalue problem is constructed, and the roots of this problem yield the axial vibration frequencies. The main novelty of this study lies in the development of a unified and generalized formulation that simultaneously accounts for bi-directional grading, deformable boundary conditions, elastic foundation interaction, and strain gradient elasticity within a single eigenvalue framework. Unlike most existing studies, which often assume idealized boundary conditions, the proposed approach allows general boundary conditions to be modeled simply by adjusting spring parameters. The model is validated through comparisons and convergence studies, and the effects of material gradation, scale parameter, elastic foundation, geometric properties, and spring stiffness are thoroughly examined.

Keywords Strain gradient theory · Bi-directionally functionally graded microbar · Longitudinal vibration · Elastic foundation · Deformable boundary conditions

1 Introduction

Functionally graded (FG) materials, which have attracted increasing interest in engineering and materials science in recent years, are advanced composite systems that exhibit continuously varying physical or chemical properties across their components. These structures, which are obtained through the controlled modification of material composition or microstructural arrangement in a specific direction, offer material systems that exhibit improved mechanical, thermal and electrical performance. This characteristic offers significant advantages for improving the performance of structural elements and has increased interest in these materials across various engineering applications. In particular, advances in nanotechnology have brought the design and application of FG materials at the nanoscale to the forefront [1]. FG structures, which allow for precise control over material distribution, pave the way for the development of multifunctional micro/nano systems. However, producing such structures at the nanoscale poses serious technical challenges, as it requires high precision and complex manufacturing processes. To overcome these challenges, micro- and nanoscale additive manufacturing (AM) techniques, developed in recent years, offer remarkable potential—especially for the fabrication of multi-material structures [2, 3]. Thanks to these advances, FG materials can now be used in a wide range of applications, including medical implants [4, 5], actuators [6], concrete [7–9], and chemical sensors [10].

Nevertheless, understanding the static and dynamic response of FG materials at the micro and nano scale remains challenging due to size-dependent behaviors and complex structural characteristics. Since conducting experiments at

Technical Editor: Geng Wang.

✉ Murat Akpınar
muratakpinar@uludag.edu.tr

Büşra Uzun
buzun@uludag.edu.tr

Mustafa Özgür Yaylı
ozguryayli@uludag.edu.tr

[1] Department of Civil Engineering, Engineering Faculty, Bursa Uludag University, Görükle Campus, 16059 Bursa, Turkey

Published online: 04 August 2026

the nano scale is technically difficult and time-consuming, researchers often rely on advanced theoretical models to study and predict the behavior of nanomaterials under static and dynamic loading. To support this theoretical approach, the static and dynamic behavior of nanostructures has been widely analyzed using advanced continuum theories that account for size-dependent effects and complex material behavior. Among these, various forms of strain gradient theory have played a key role in capturing small-scale effects often neglected by classical models and in improving the modeling accuracy of nanostructures under both static and dynamic loading conditions. Notable examples include the classical strain gradient theory (SGT) proposed by Aifantis [11, 12], the nonlocal strain gradient theory (NSGT) introduced by Lim et al. [13], and the modified strain gradient theory (MSGT) developed by Lam et al. [14]. The SGT reflects a hardening behavior, which results in increased natural frequencies and critical buckling loads, along with reduced bending deformation. In contrast, the NSGT can represent both hardening and softening effects; in this theory, higher values of the nonlocal parameter tend to lower the natural frequencies, while greater material length scale parameters (MLSPs) lead to an increase. Additionally, the MSGT (or Lam strain gradient theory) introduces three independent MLSPs, offering a more refined modeling capability compared to classical approaches. In this context, the free transverse vibration analyses of various structures have been presented in the literature by researchers, including: a FG nanobeam with a tip nanoparticle and nonlinear/linear spring constraints using the SGT [15]; a FG-porous microbeam under thermal effects using the MSGT [16]; fluid-conveying nanotubes analyzed using the SGT combined with inertia gradients [17]; Timoshenko microbeams based on MSGT and von Kármán theory [18]; and beams subjected to thermal effects using the SGT [19]. Moreover, other studies have further investigated the transverse vibration characteristics of micro/nanostructures [20–23], enriching the overall understanding of their dynamic behavior.

In addition, these theories are also frequently employed in buckling and bending analyses. In this context, several studies have been presented in the literature, including: buckling analysis of FG microbeams based on MSGT [24]; thermally affected microbeams analyzed using MSGT [25]; axially loaded cantilever nanobeams with intermediate supports using SGT [26]; gradient elastic beams modeled using SGT and finite element methods [27]; and finally, a generally supported microbeam based on surface energy–enhanced SGT [28]. Furthermore, several investigations have been conducted within the framework of MSGT, focusing on the bending response of various micro/nanostructures. These include: single-walled carbon nanotubes (CNTs) within an elastic medium [29]; microbeams analyzed using MSGT [30]; simply supported FG microbeams interacting with a Winkler–Pasternak foundation framework based on MSGT [31]; and FG microbeams under simply supported conditions and placed in a Winkler-type elastic media examined through MSGT-based modeling approaches [32]. Moreover, Akgöz and Civalek [33] analyzed the buckling of nonhomogeneous, tapered FG microbeams using MSGT. In addition to the aforementioned studies, several works have focused on both the bending and vibration behaviors of micro/nanostructures [34–38], while others have provided a more comprehensive investigation encompassing bending, vibration, and buckling analyses within unified theoretical frameworks [39–44].

In addition to bending, buckling, and transverse vibration, these theories are also frequently used to analyze torsional and longitudinal vibrations of micro- and nanoscale structures. Within this context, Barretta et al. [45] studied the torsional oscillations of FG nanobeams using nonlocal Lam's strain gradient theory (NL-LSGT). In the following studies, Kafkas et al. [46] explored torsional oscillations of a FG circular nanobeam with both ends constrained by torsion springs, while Akpınar et al. [47] studied the torsional oscillations of a porous nanorod under similar boundary conditions, based on the NL-LSGT. Noroozi et al. [48] presented the torsional vibration analysis of a nonlinear bi-directional functionally graded (BD-FG) nano-cone, while Guo et al. [49] studied the torsional oscillations of a CNT, taking into account the axial velocity and velocity gradient effects based on the NSGT. Uzun et al. [50] studied the torsional oscillations of FG-porous nanotubes with deformable springs at both ends based on MSGT. Similar to these works, other studies can also be found in the literature that investigate the torsional vibrations of nano/micro structures using different strain gradient theories [51–56].

Moreover, the axial vibration of a bar with various boundary conditions was analyzed on the basis of SGT by Altan et al. [57]. In subsequent studies, Kahrobaiyan et al. [58] studied the longitudinal vibration of microbars using the MSGT. Akgöz and Civalek explored the longitudinal free vibration of homogeneous microbars [59] and axially FG microbars [60] under both clamped and unclamped boundary conditions using the MSGT. Dimosthenis [61] analytically presented the longitudinal free vibration behavior of a bar with free, clamped, attached mass, and/

or spring boundary conditions using the SGT. Based on the NSGT, Şimşek [62] examined the axial vibration behavior of a nanorod embedded in an elastic medium, while Li et al. [63] investigated a similar problem for a nanorod in free space. In line with these studies, several other works in the literature also explore the longitudinal vibration of nano- and micro-scale structures [64–76].

In this study, a comprehensive formulation for the axial vibration analysis of BD-FG microbars is developed within the framework of SGT. First, the governing equation of motion in the axial direction and the corresponding boundary conditions are derived using Hamilton's principle. The axial displacement field is expressed by a Fourier sine series. The Stokes' transform is then applied to impose the boundary conditions in a flexible manner, without requiring the displacement function to satisfy them exactly. Finally, all model parameters, including material gradation, strain gradient effects, elastic foundation stiffness, and boundary spring constants, are collected into an eigenvalue matrix. The natural frequencies of the system are obtained by setting the determinant of this matrix equal to zero. Unlike many conventional approaches that assume perfectly rigid or free boundaries, the present formulation accounts for boundary flexibility by introducing axial springs at both ends. By varying the spring stiffness parameters, different boundary conditions can be modeled within a unified framework, which extends existing FG microbar vibration models and enables a more realistic analysis of deformable supports.

2 Material property variation in bi-directionally functionally graded microbars

This research focuses on the longitudinal vibration behavior of a BD-FG microbar constrained by axial springs and embedded in an elastic foundation, as depicted in Fig. 1. The BD-FG microbar with a length of L is composed of a functionally graded mixture of ceramic and metal constituents. Its mechanical properties vary continuously along both the width (b) and thickness (h) directions. This spatial variation in material properties can be described as follows [77, 78]:

$$f(y,z) = f_c V_c(y,z) + f_m V_m(y,z) \tag{1}$$

Here, $f(y,z)$ denotes the material property of the BD-FG microbar, incorporating the properties of both metal (f_m) and ceramic (f_c). Also, $V_m(y,z)$ and $V_c(y,z)$ represent the volume fractions of metal and ceramic, respectively, and they satisfy the following relationship:

$$V_m(y,z) = 1 - V_c(y,z) \tag{2}$$

In a BD-FG microbar, material properties vary along both the y- and z-axes. In such structures, the outer surface predominantly exhibits ceramic characteristics, while the inner region reflects the dominant properties of metal. The volume fraction of ceramic in the aforementioned equation is determined as follows [77, 78]:

$$V_c(y,z) = \left[1 - \left(\left|\frac{2y}{b}\right| - 1\right)\right]^n \left[1 - \left(\left|\frac{2z}{h}\right| - 1\right)\right]^p \tag{3}$$

The material gradation in the BD-FG microbar is characterized by the material grading coefficients n and p, where n represents the material grading coefficient in the y-direction and p corresponds to the material grading coefficient in the z-direction. When $n > 0 \,\&\, p > 0$, the material properties exhibit gradation in both the width and thickness directions. If $p = 0$, the material properties vary exclusively along the width direction (the y-axis), while when $n = 0$, the properties change only in the thickness direction (the z-axis). In the case where $n = p = 0$, the beam consists entirely of ceramic material, whereas for $n = p = \infty$, the

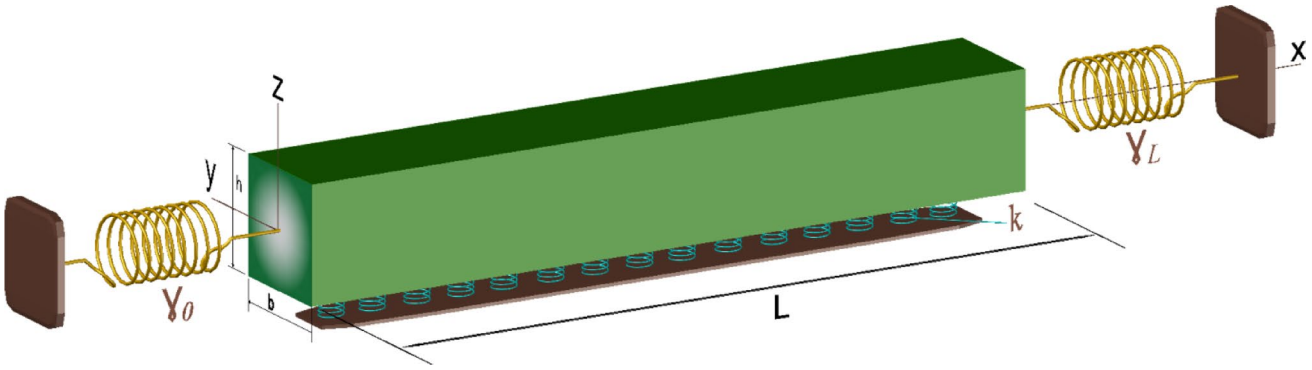


Fig. 1 BD-FG microbar model supported by axial springs

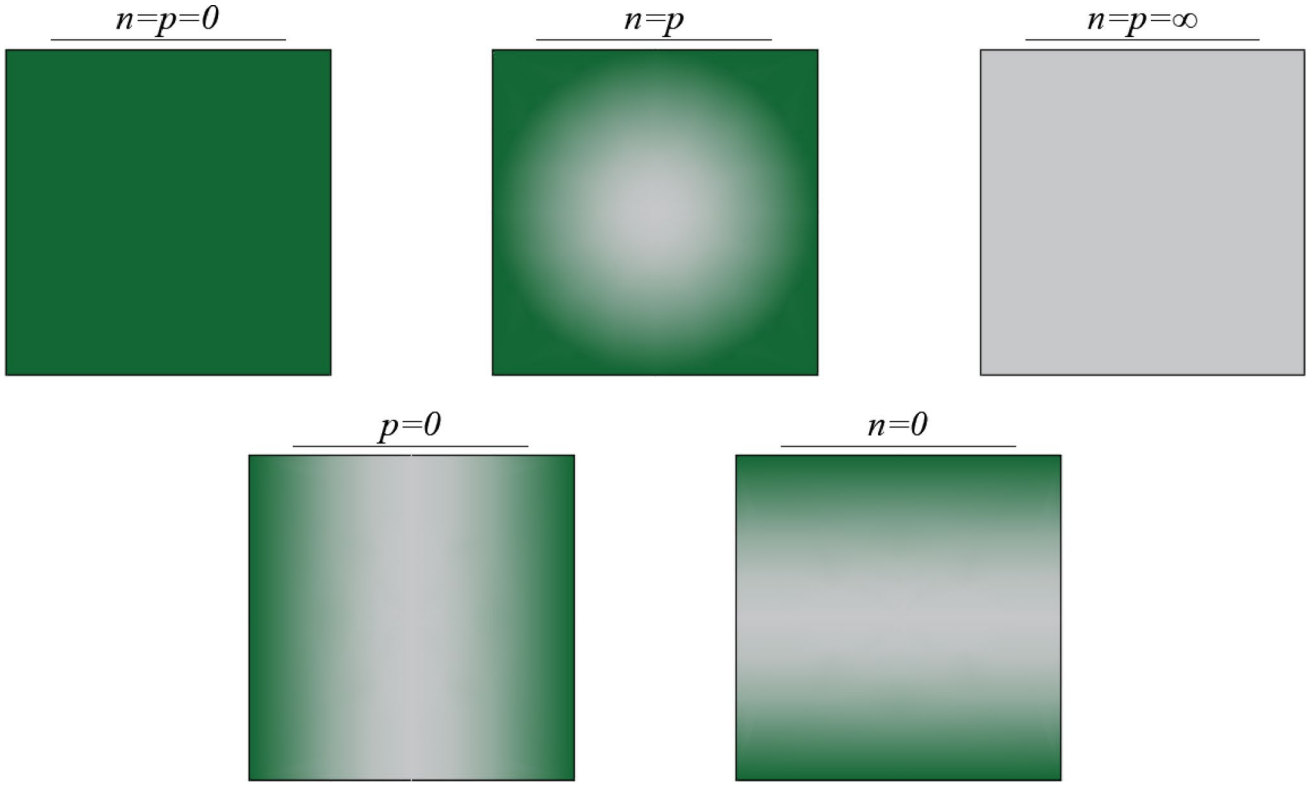


Fig. 2 Material property variation of the BD-FG microbar under different grading parameter conditions

beam is entirely metallic. These variations are visually represented in Fig. 2. In this figure, the green regions represent the ceramic phase, while the gray regions correspond to the metallic phase. Using the equations derived above, the effective material properties of the BD-FG microbar can be given as follows:

$$f(y,z) = f_m + (f_c - f_m)\left[1 - \left(\left|\frac{2y}{b}\right| - 1\right)\right]^n \left[1 - \left(\left|\frac{2z}{h}\right| - 1\right)\right]^p \tag{4}$$

Using Eq. (4), the effective elasticity modulus $E(y,z)$ and mass density $\rho(y,z)$ of the BD-FG microbar are determined as follows, respectively:

$$E(y,z) = E_m + (E_c - E_m)\left[1 - \left(\left|\frac{2y}{b}\right| - 1\right)\right]^n \left[1 - \left(\left|\frac{2z}{h}\right| - 1\right)\right]^p \tag{5}$$

$$\rho(y,z) = \rho_m + (\rho_c - \rho_m)\left[1 - \left(\left|\frac{2y}{b}\right| - 1\right)\right]^n \left[1 - \left(\left|\frac{2z}{h}\right| - 1\right)\right]^p \tag{6}$$

It should be noted that at micro- and nano-scales, interfacial effects, porosity, and microstructural heterogeneity may affect the effective properties. In such cases, advanced homogenization methods (e.g., Mori–Tanaka, self-consistent, or multiscale schemes) can provide improved accuracy by accounting for phase interactions and microstructure.

3 Derivation of the governing equation using strain gradient theory

The linear elastic constitutive relations proposed by Aifantis et al. [11, 12], including the Cauchy stress tensor σ_{ij}, the fourth-order elasticity tensor C_{ijkl}, the strain tensor ε_{kl}, the Laplacian of the strain tensor $\varepsilon_{kl,mm}$, and the MLSP μ, are derived as follows:

$$\sigma_{ij} = C_{ijkl}\left(\varepsilon_{kl} - \mu^2 \varepsilon_{kl,mm}\right) \tag{7}$$

The parameter μ represents an intrinsic material length (material length scale parameter) related to microstructural features (e.g., grain size). In FG materials, the scale parameter may also vary spatially, and there are studies that model this variation [33, 79]. In the present work, μ is assumed uniform to keep the model simple and isolate the

effect of property grading, while future studies could use a spatially varying $\mu(x, z)$ linked to local composition.

Furthermore, it is acknowledged that more comprehensive theories, such as the MSGT [14] or NSGT [13], introduce additional length scales and can capture a wider range of size-dependent effects. While the qualitative stiffening trend observed here is consistent with these advanced models, quantitative results would differ depending on the additional parameters they employ. Therefore, the present results should be interpreted within the context of the chosen single-parameter gradient model. Future work could extend this analysis to compare predictions across different gradient elasticity formulations. The strain energy density now includes classical and gradient terms, written as [11, 80]:

$$U = \frac{1}{2}\lambda\varepsilon_{ii}\varepsilon_{jj} + \vartheta\varepsilon_{ij}\varepsilon_{ij} + \mu^2\left(\frac{1}{2}\lambda\varepsilon_{ii,k}\varepsilon_{jj,k} + \vartheta\varepsilon_{ij,k}\varepsilon_{ij,k}\right) \tag{8}$$

where,

$$\varepsilon_{ij} = \frac{1}{2}\left(u_{i,j} + u_{j,i}\right) \tag{9}$$

Here, λ and ϑ denote the Lamé constants. In addition, when $\mu = 0$ is applied, the proposed bar model simplifies to the classical model. The strain energy density function U, which includes the stress (σ, σ_x) and strain $(\varepsilon, \varepsilon_x)$ tensors expressions, is given for the microbar model as follows [61]:

$$U = \frac{1}{2}\int_0^L \left(\sigma\varepsilon + \sigma_x\varepsilon_x\right) A dx \tag{10}$$

where,

$$\sigma = E\frac{du(x,t)}{dx} \tag{11}$$

$$\sigma_x = \mu^2 E\frac{d^2u(x,t)}{dx^2} \tag{12}$$

$$\varepsilon = \frac{du(x,t)}{dx} \tag{13}$$

$$\varepsilon_x = \frac{d^2u(x,t)}{dx^2} \tag{14}$$

Here, A is the cross-section area of the microbar. It should be noted that the present model assumes linear elastic material behavior, small strains, and moderate displacements, so that geometric nonlinearity is negligible [81, 82]. At micro- and nano-scales, geometric and material nonlinearities may become significant, making the linear model inadequate for large-amplitude vibrations [82]. Future extensions of this work could, therefore, incorporate nonlinear kinematics (e.g., using the von Kármán strain–displacement relations) and/or nonlinear constitutive models into the current strain gradient elasticity framework to capture these effects. Moreover, in this study, the governing equation and boundary conditions are established through Hamilton's principle, which is given by the following equation:

$$\int_{t_1}^{t_2} \delta\left(U - T\right) dt - \int_{t_1}^{t_2} \delta W dt = 0 \tag{15}$$

By substituting the expressions defined in Eqs. (11)–(14) into Eq. (10), the strain energy expression (U) can be expressed as:

$$U = \frac{1}{2}\int_0^L \left\{A_E\left(\frac{du(x,t)}{dx}\right)^2 + \mu^2 A_E\left(\frac{d^2u(x,t)}{dx^2}\right)^2\right\} dx \tag{16}$$

Moreover, the kinetic energy expression (T) is represented by the equation below:

$$T = \frac{1}{2}\int_0^L A_\rho\left(\frac{du(x,t)}{dt}\right)^2 dx \tag{17}$$

The expressions A_E and A_ρ in the above equations are derived as follows:

$$A_E = \int_{-h/2}^{h/2}\int_{-b/2}^{b/2} E\left(y, z\right) dydz \tag{18}$$

$$A_\rho = \int_{-h/2}^{h/2}\int_{-b/2}^{b/2} \rho\left(y, z\right) dydz \tag{19}$$

Finally, the work done by external forces (W) is defined as follows:

$$\delta W = \int_0^L F\delta u dx + [P\delta u]_0^L + \left[D\delta\frac{du}{dx}\right]_0^L \tag{20}$$

where,

$$F = -k_e u \tag{21}$$

Here, t represents time, k_e refers to the elastic foundation stiffness coefficient. Also, P and D represent the conventional and higher-order axial resultants, respectively. By combining Eqs. (16) and (17), the first integral is derived as follows, according to the principles of variational calculus [61]:

$$\begin{aligned}\int_{t_1}^{t_2}\delta(U-T)\,dt &= \int_{t_1}^{t_2}\int_0^L \delta R(u_x, u_{xx}, \dot{u})\,dxdt \\ &= \int_{t_1}^{t_2}\left\{\int_0^L\left[\frac{\partial^2}{\partial x^2}\left(\frac{\partial R}{\partial u_{xx}}\right) - \frac{\partial}{\partial x}\left(\frac{\partial R}{\partial u_x}\right) - \frac{\partial}{\partial t}\left(\frac{\partial R}{\partial \dot{u}}\right)\right]\delta u dx\right\}dt \\ &+ \int_{t_1}^{t_2}\left[\left[\frac{\partial R}{\partial u_x} - \frac{\partial}{\partial x}\left(\frac{\partial R}{\partial u_{xx}}\right)\right]\delta u + \frac{\partial R}{\partial u_{xx}}\delta u'\right]_0^L dt \\ &+ \int_0^L\left[\frac{\partial R}{\partial \dot{u}}\delta u\right]_{t_1}^{t_2} dx\end{aligned} \tag{22}$$

The Lagrangian function, as given in Eq. (22), is expressed as follows:

$$R = \frac{A_E}{2}(u_x)^2 + \mu^2\frac{A_E}{2}(u_{xx})^2 - \frac{A_\rho}{2}(\dot{u})^2 \tag{23}$$

where,

$$u_x = \frac{du}{dx} \tag{24}$$

$$u_{xx} = \frac{d^2u}{dx^2} \tag{25}$$

$$\dot{u} = \frac{du}{dt} \tag{26}$$

Using Eqs. (24)–(26), Eq. (22) can be expressed as follows:

$$\begin{aligned}\int_{t_1}^{t_2}\delta(U-T)dt &= \int_{t_1}^{t_2}\left\{\int_0^L\left[\mu^2A_E u_{xxxx} - A_E u_{xx} + A_\rho\ddot{u}\right]\delta u dx\right\}dt \\ &+ \int_{t_1}^{t_2}\left[\left(A_E u_x - \mu^2A_E u_{xxx}\right)\delta u + \mu^2A_E u_{xx}\delta u'\right]_0^L dt \\ &+ \int_0^L\left[A_\rho\dot{u}\delta u\right]_{t_1}^{t_2} dx\end{aligned} \tag{27}$$

The second integral is derived according to the principles of variational calculus, as shown below [61]:

$$\int_{t_1}^{t_2}\delta W dt = \int_{t_1}^{t_2}\int_0^L F\delta u dx dt + \int_{t_1}^{t_2}\left\{[P\delta u]_0^L + [Q\delta u']_0^L\right\}dt \tag{28}$$

Employing Eqs. (27) and (28) through Hamilton's variational approach yields the following equation:

$$\begin{aligned}&\left(\int_{t_1}^{t_2}\left\{\int_0^L\left[\mu^2A_E u_{xxxx} - A_E u_{xx} + A_\rho\ddot{u}\right]\delta u dx\right\}dt\right. \\ &+ \left.\int_{t_1}^{t_2}\left[\left(A_E u_x - \mu^2A_E u_{xxx}\right)\delta u + \mu^2A_E u_{xx}\delta u'\right]_0^L dt + \int_0^L\left[A_\rho\dot{u}\delta u\right]_{t_1}^{t_2}\right) \\ &- \left(\int_{t_1}^{t_2}\int_0^L F\delta u dx dt + \int_{t_1}^{t_2}\left\{[P\delta u]_0^L + [Q\delta u']_0^L\right\}dt\right)\end{aligned} \tag{29}$$

Therefore, the vibration equation for an FG microbar is derived in the following form [61]:

$$A_E\frac{\partial^2u}{\partial x^2} - \mu^2A_E\frac{\partial^4u}{\partial x^4} + F - A_\rho\frac{\partial^2u}{\partial t^2} = 0 \tag{30}$$

Furthermore, based on Eq. (29), the boundary conditions for the microbar are expressed as below [61]:

$$P = A_E\frac{du}{dx} - \mu^2A_E\frac{\partial^3u}{\partial x^3} \quad or \quad \delta u = 0 \quad at \quad x = 0, L \tag{31}$$

$$Q = \mu^2A_E\frac{\partial^2u}{\partial x^2} \quad or \quad \delta u\prime = 0 \quad at \quad x = 0, L \tag{32}$$

The governing equation and boundary conditions correspond to a conservative system and therefore do not include damping. In practical MEMS/NEMS applications, energy dissipation mechanisms such as material viscoelasticity, air damping, or foundation losses can significantly affect the dynamic response. In future work, damping can be incorporated by adding viscous or viscoelastic terms, e.g., using a Kelvin–Voigt type model.

4 Multi-parameter eigenvalue formulation for axial vibration

This chapter presents a methodology for analyzing the longitudinal vibration of a BD-FG microbar resting on an elastic foundation, which involves an eigenvalue problem. The eigenvalue problem is formulated in its most general form, incorporating spring coefficients at the boundaries, material property variations, scale parameters, and elastic foundation stiffness coefficients. The deformable boundary

conditions associated with this problem are derived using Fourier infinite series and Stokes' transforms. According to the proposed solution method, the displacement function $u\,(x,t)$ is expressed in terms of $\varphi(x)$ by separating the time variable t, as follows [72]:

$$u\,(x,t) = \varphi(x)e^{i\omega t} \tag{33}$$

Thanks to this discretization, the governing equation can be reformulated to explicitly incorporate the natural frequencies (ω), as follows:

$$A_E\varphi(x)'' - \mu^2 A_E\varphi\,(x)^{(4)} - k_e\varphi\,(x) + A_\rho\omega^2\varphi\,(x) = 0 \tag{34}$$

The displacement function is expressed using a Fourier sine series, allowing the description of the nanotube's behavior both at the boundaries ($x = 0$ and $x = L$) and within the region between them $(0 < x < L)$, as shown below [72]:

$$\varphi\,(x) = \begin{cases} \varphi_0, x = 0, \\ \varphi_L, x = L, \\ \sum_{r=1}^{\infty} b_r sin\,(\beta_r x)\,, 0 < x < L \end{cases} \tag{35}$$

In this context, the equation $\beta_r = r\pi/L$ holds, and b_r denotes the Fourier coefficient, which is calculated as follows:

$$b_r = \frac{2}{L}\int_0^L \varphi(x) sin\,(\beta_r x)\,dx \tag{36}$$

By applying Stokes' transforms, the derivatives of the displacement function are represented using a Fourier series. In this framework, the first derivative associated with Eq. (35) is formulated as follows:

$$\varphi\prime\,(x) = \sum_{r=1}^{\infty} \beta_r b_r cos\,(\beta_r x) \tag{37}$$

If Eq. (37) is rewritten in the form of a cosine series, then the following expression is obtained:

$$\varphi\prime\,(x) = \frac{c_0}{L} + \sum_{r=1}^{\infty} c_r cos\,(\beta_r x) \tag{38}$$

The coefficients c_0 and c_r of the Fourier series, obtained from the preceding equation, can be expressed as follows:

$$c_0 = \frac{2}{L}\int_0^L \varphi\prime\,(x)\,dx = \frac{2}{L}\,(\varphi_L - \varphi_0) \tag{39}$$

$$c_r = \frac{2}{L}\int_0^L \varphi\prime\,(x)\,cos\,(\beta_r x)\,dx, (r = 1,2,\dots) \tag{40}$$

The Fourier coefficient c_r obtained earlier can be calculated using integration by parts, as illustrated below:

$$c_r = \frac{2}{L}[\varphi\,(x)\,cos\,(\beta_r x)]_0^L + \frac{2}{L}\left[\beta_r\int_0^L \varphi\,(x)\,sin\,(\beta_r x)\,dx\right] \tag{41}$$

$$c_r = \frac{2(-1)^r\,(\varphi_L - \varphi_0)}{L} + \beta_r b_r \tag{42}$$

Using Stokes transforms, the first six derivatives of $\varphi\,(x)$ can be derived as follows [72]:

$$\varphi\prime\,(x) = \frac{(\varphi_L - \varphi_0)}{L} + \sum_{r=1}^{\infty} cos\,(\beta_r x)\left(\frac{2\,[(-1)^r\varphi_L - \varphi_0]}{L} + \beta_r b_r\right) \tag{43}$$

$$\varphi''\,(x) = -\sum_{r=1}^{\infty} \beta_r sin\,(\beta_r x)\left(\frac{2\,[(-1)^r\varphi_L - \varphi_0]}{L} + \beta_r b_r\right) \tag{44}$$

$$\begin{aligned}\varphi'''\,(x) = {} & \frac{\varphi_L'' - \varphi_0''}{L} \\ & + \sum_{r=1}^{\infty} cos\,(\beta_r x)\left[\frac{2\,[\varphi_L''\,(-1)^r - \varphi_0'']}{L}\right. \\ & \left. - \beta_r^2\left(\frac{2\,[(-1)^r\,\varphi_L - \varphi_0]}{L} + \beta_r b_r\right)\right]\end{aligned} \tag{45}$$

$$\begin{aligned}\varphi^{(4)}(x) = {} & -\sum_{r=1}^{\infty} \beta_r sin\,(\beta_r x) \\ & \left[\frac{2\,[\varphi_L''\,(-1)^r - \varphi_0'']}{L} - \beta_r^2\left(\frac{2\,[(-1)^r\,\varphi_L - \varphi_0]}{L} + \beta_r b_r\right)\right]\end{aligned} \tag{46}$$

By inserting Eqs. (35), (44), and (46) into Eq. (34), the coefficient b_r is determined as follows:

$$b_r = \frac{2\beta_r \left[\left(A_E + A_E\mu^2\beta_r^2\right)\varphi_0 - (-1)^r\left(A_E + A_E\mu^2\beta_r^2\right)\varphi_L - A_E\mu^2\left(\varphi_0'' - \varphi_L''(-1)^r\right)\right]}{L(k_e - A_\rho\omega^2 + A_E\beta_r^2 + A_E\mu^2\beta_r^4)} \tag{47}$$

This method, derived using Stokes' transforms and Fourier series, enables a continuous transition from clamped–clamped (C–C) to clamped–free (C–F) boundary conditions through appropriate tuning of the stiffness coefficients of the springs located at the boundaries. Furthermore, by assigning intermediate stiffness values, boundary deformations that are rarely examined in the literature can also be investigated, without the need to reformulate the solution procedure. In addition, the deformable force boundary conditions can be expressed as follows:

$$A_E\frac{du}{dx} - \mu^2 A_E\frac{\partial^3 u}{\partial x^3}\bigg|_{x=0} = \gamma_0\varphi_0 \tag{48}$$

$$A_E\frac{du}{dx} - \mu^2 A_E\frac{\partial^3 u}{\partial x^3}\bigg|_{x=L} = -\gamma_L\varphi_L \tag{49}$$

Here, γ_0 and γ_L represent the spring coefficients located at the ends of the BD-FG microbar. Assigning sufficiently large values to these coefficients results in rigid boundary behavior, while assigning very small values leads to free-end conditions. To formulate the corresponding eigenvalue problem, Eqs. (43), (45), and (47) are substituted into Eqs. (48) and (49) as follows:

$$\begin{aligned}&\left(-\gamma_0 - \frac{A_E}{L} - \sum_{r=1}^{\infty}\frac{2LA_E\left(k_e - A_\rho\omega^2\right)\left(L^2 + r^2\pi^2\mu^2\right)}{k_eL^4 + A_Er^2\pi^2\left(L^2 + r^2\pi^2\mu^2\right) - L^4A_\rho\omega^2}\right)\varphi_0\\ &+\left(\frac{A_E}{L} + \sum_{r=1}^{\infty}\frac{2L(-1)^rA_E\left(k_e - A_\rho\omega^2\right)\left(L^2 + r^2\pi^2\mu^2\right)}{k_eL^4 + A_Er^2\pi^2\left(L^2 + r^2\pi^2\mu^2\right) - L^4A_\rho\omega^2}\right)\varphi_L = 0\end{aligned} \tag{50}$$

$$\begin{aligned}&\left(\frac{A_E}{L} + \sum_{r=1}^{\infty}\frac{2L(-1)^rA_E\left(k_e - A_\rho\omega^2\right)\left(L^2 + r^2\pi^2\mu^2\right)}{k_eL^4 + A_Er^2\pi^2\left(L^2 + r^2\pi^2\mu^2\right) - L^4A_\rho\omega^2}\right)\varphi_0\\ &+\left(-\gamma_L - \frac{A_E}{L} - \sum_{r=1}^{\infty}\frac{2LA_E\left(k_e - A_\rho\omega^2\right)\left(L^2 + r^2\pi^2\mu^2\right)}{k_eL^4 + A_Er^2\pi^2\left(L^2 + r^2\pi^2\mu^2\right) - L^4A_\rho\omega^2}\right)\varphi_L = 0\end{aligned} \tag{51}$$

Based on Eqs. (50) and (51), the following eigenvalue problem is formulated, taking into account the influences of spring stiffness, elastic foundation stiffness coefficients, material characteristics, and scale-dependent effects:

$$\det\begin{bmatrix}\psi_{11} & \psi_{12}\\ \psi_{21} & \psi_{22}\end{bmatrix} = 0 \tag{52}$$

where,

$$\psi_{11} = -\gamma_0 - \frac{A_E}{L} - \sum_{r=1}^{\infty}\frac{2LA_E\left(k_e - A_\rho\omega^2\right)\left(L^2 + r^2\pi^2\mu^2\right)}{k_eL^4 + A_Er^2\pi^2\left(L^2 + r^2\pi^2\mu^2\right) - L^4A_\rho\omega^2} \tag{53}$$

$$\psi_{12} = \frac{A_E}{L} + \sum_{r=1}^{\infty}\frac{2L(-1)^rA_E\left(k_e - A_\rho\omega^2\right)\left(L^2 + r^2\pi^2\mu^2\right)}{k_eL^4 + A_Er^2\pi^2\left(L^2 + r^2\pi^2\mu^2\right) - L^4A_\rho\omega^2} \tag{54}$$

$$\psi_{21} = \frac{A_E}{L} + \sum_{r=1}^{\infty}\frac{2L(-1)^rA_E\left(k_e - A_\rho\omega^2\right)\left(L^2 + r^2\pi^2\mu^2\right)}{k_eL^4 + A_Er^2\pi^2\left(L^2 + r^2\pi^2\mu^2\right) - L^4A_\rho\omega^2} \tag{55}$$

$$\psi_{22} = -\gamma_L - \frac{A_E}{L} - \sum_{r=1}^{\infty}\frac{2LA_E\left(k_e - A_\rho\omega^2\right)\left(L^2 + r^2\pi^2\mu^2\right)}{k_eL^4 + A_Er^2\pi^2\left(L^2 + r^2\pi^2\mu^2\right) - L^4A_\rho\omega^2} \tag{56}$$

This study introduces a novel eigenvalue formulation that explicitly accounts for possible boundary deformations—an aspect that has received limited attention in prior research on

Table 1 Comparison of DFs in the first three modes under different elastic foundation stiffness coefficients ($\gamma_0 = \gamma_L = 10^{14}$ nN/nm)

$\frac{\mu}{L}$	k	*First mode*		*Second mode*		*Third mode*	
		Present	*Şimşek* [62]	*Present*	*Şimşek* [62]	*Present*	*Şimşek* [62]
0.0	*0*	3.1415	3.1415	6.2831	6.2831	9.4247	9.4247
	1	3.2969	3.2969	6.3622	6.3622	9.4776	9.4776
	5	3.8561	3.8561	6.6692	6.6692	9.6864	9.6864
	10	4.4575	4.4575	7.0340	7.0340	9.9411	9.9411
0.25	*0*	3.9947	3.9947	11.6999	11.699	24.1238	24.123
	1	4.1179	4.1179	11.7426	11.742	24.1446	24.144
	5	4.5779	4.5779	11.9117	11.911	24.2273	24.227
	10	5.0948	5.0948	12.1197	12.119	24.3302	24.330
0.5	*0*	5.8499	5.8499	20.7151	20.715	45.4022	45.402
	1	5.9348	5.9348	20.7392	20.739	45.4132	45.413
	5	6.2627	6.2627	20.8354	20.835	45.4572	45.457
	10	6.6499	6.6499	20.9551	20.955	45.5122	45.512
1.0	*0*	10.3575	10.357	39.9753	39.975	89.325	89.325
	1	10.4057	10.405	39.9878	39.987	89.330	89.330
	5	10.5962	10.596	40.0378	40.037	89.353	89.353
	10	10.8295	10.829	40.1002	40.100	89.381	89.380

nano- and microscale systems. Unlike conventional models that assume perfectly rigid or completely free boundaries, this approach recognizes that even slight boundary flexibility can significantly influence the dynamic behavior of small-scale structures. To address this, deformable springs are placed at both ends of the BD-FG microbar. A main contribution of this study is its ability to model a wide range of boundary conditions by changing the stiffness of the springs. This flexible modeling approach improves the physical accuracy of the analysis and offers a clear improvement over traditional boundary assumptions, making it more useful for real-world nanoscale engineering problems.

5 Numerical results

In this section of the study, the factors influencing the longitudinal vibration behavior of BD-FG microbars—such as material properties, spring stiffness parameters, elastic foundation effects, and size-dependent characteristics—are examined. To verify the accuracy of the proposed method, comparative results are presented in the first three tables. Table 1 provides a comparison of the dimensionless frequencies (DFs) of a homogeneous microbar under varying MLSPs and elastic foundation stiffness coefficients, with the results reported by Şimşek [62]. In this study, the DFs, denoted by $\overline{\omega}$, are calculated using the following formula:

$$\overline{\omega} = \omega L \sqrt{\frac{\rho_c}{E_c}} \tag{57}$$

Additionally, the elastic foundation stiffness coefficient is also treated in a dimensionless form and is calculated using the following expression:

$$k = \frac{k_e L^2}{E_c A} \tag{58}$$

Şimşek [62] investigated the axial vibration of a fixed–fixed nanorod using the nonlocal strain gradient theory (NSGT). When the nonlocal effects are omitted from Şimşek's [62] study, his model becomes comparable to the one proposed in this work. In the current study, the boundary conditions employed in Şimşek's [62] model can be reproduced by assigning a spring stiffness value of 10^{14} nN/nm at both ends of the microbar. The comparison in Table 1 clearly demonstrates that the results obtained using the proposed method are in excellent agreement with those in the literature, thus validating the accuracy and reliability of the approach.

Unless otherwise stated, the same parameter values are used throughout the study in the tables and figures following Table 3. These are as follows: $b = h = 1\ \mu m$, $L = 20\text{h}\ \mu m$, $n = p = 2$, $k = 10$, $\mu = 1h$, and $\gamma_0 = \gamma_L = 10^{14}$ nN/nm. Additionally, the number of terms considered in the Fourier series expansion is taken as $r = 10$. The elastic modulus and mass density of the BD-FG material are selected based on the work of Vel [83]. In this context, silicon carbide (SiC) is chosen as the ceramic phase, and titanium (Ti) as the metallic phase of the BD-FG microbar. SiC is characterized by an elastic modulus of 410 GPa and a mass density of 3100 kg/m^3, whereas Ti has an elastic modulus of 105.8 GPa and a mass density of 4420 kg/m^3.

Table 2 Comparison of DFs for different boundary conditions and mode numbers ($\mu = 0$)

k	*Mode number*	$\gamma_0 = \gamma_L = 10^{14}$ nN/nm *(C–C)*			$\gamma_0 = 10^{14}$ nN/nm & $\gamma_L = 10^{-6}$ nN/nm *(C–F)*		
		Present	*FEM* [73]	*Analytical* [73]	*Present*	*FEM* [73]	*Analytical* [73]
0	*1*	3.1415	3.14303	3.14159	1.5729	1.57098	1.57080
	2	6.2831	6.29468	6.28319	4.7187	4.71724	4.71239
	3	9.4247	9.46358	9.42478	7.8645	7.87643	7.85398
	4	12.5664	12.65843	12.56637	11.0104	11.05722	10.99557
5	*1*	3.8561	3.8573	3.8561	2.7338	2.7328	2.7327
	2	6.6692	6.6800	6.6692	5.2217	5.2204	5.2160
	3	9.6864	9.7242	9.6864	8.1762	8.1877	8.1661
	4	12.7638	12.8544	12.7638	11.2352	11.2811	11.2206
50	*1*	7.7375	7.7381	7.7376	7.2439	7.2435	7.2434
	2	9.4593	9.4669	9.4593	8.5009	8.5001	8.4974
	3	11.7825	11.8135	11.7825	10.5760	10.5848	10.5681
	4	14.4192	14.4995	14.4192	13.0854	13.1249	13.0730
100	*1*	10.4819	10.4823	10.4819	10.1229	10.1226	10.5681
	2	11.8101	11.8162	11.8101	11.0574	11.0568	11.0547
	3	13.7414	13.7681	13.7414	12.7221	12.7294	12.7155
	4	16.0597	16.1318	16.0597	14.8738	14.9085	14.8628

Table 3 Convergence study of DFs considering boundary conditions, elastic foundations, and MLSPs

k	$\frac{\mu}{h}$	$\gamma_0 = \gamma_L = 10^{14}$ nN/nm *(C–C)*				$\gamma_0 = 10^{14}$ nN/nm & $\gamma_L = 10^{-6}$ nN/nm *(C–F)*			
		Analytical Equation (59)	*Fourier Solution*			*Analytical Equation (60)*	*Fourier Solution*		
			n=30	*n=20*	*n=10*		*n=150*	*n=100*	*n=30*
10	*0*	4.4575	4.4575	4.4575	4.4575	3.5309	3.5318	3.5323	3.5356
	0.5	4.4847	4.4847	4.4847	4.4847	3.5330	3.5338	3.5343	3.5376
	1.0	4.5654	4.5654	4.5654	4.5654	3.5395	3.5388	3.5393	3.5428
	1.5	4.6969	4.6969	4.6969	4.6969	3.5502	3.5455	3.5461	3.5497
	2.0	4.8750	4.8750	4.8750	4.8750	3.5652	3.5529	3.5534	3.5574
	2.5	5.0948	5.0948	5.0948	5.0948	3.5844	3.5601	3.5607	3.5648
50	*0*	7.7375	7.7375	7.7375	7.7375	7.2434	7.2439	7.2441	7.2457
	0.5	7.7532	7.7532	7.7532	7.7532	7.2444	7.2448	7.2451	7.2467
	1.0	7.8002	7.8002	7.8002	7.8002	7.2476	7.2473	7.2475	7.2492
	1.5	7.8779	7.8779	7.8779	7.8779	7.2528	7.2506	7.2508	7.2526
	2.0	7.9853	7.9853	7.9853	7.9853	7.2602	7.2542	7.2545	7.2564
	2.5	8.1214	8.1214	8.1214	8.1214	7.2696	7.2577	7.2580	7.2600
100	*0*	10.481	10.481	10.481	10.481	10.1226	10.1229	10.1231	10.1243
	0.5	10.4935	10.4935	10.4935	10.4935	10.1234	10.1236	10.1238	10.1250
	1.0	10.5282	10.5282	10.5282	10.5282	10.1256	10.1254	10.1255	10.1268
	1.5	10.5859	10.5859	10.5859	10.5859	10.1294	10.1277	10.1279	10.1292
	2.0	10.6661	10.6661	10.6661	10.6661	10.1346	10.1303	10.1305	10.1319
	2.5	10.7684	10.7684	10.7684	10.7684	10.1414	10.1328	10.1330	10.1345

In Table 2, the dimensionless frequencies (DFs) obtained in this study are compared with the results reported by Civalek et al. [73], who presented both finite element method (FEM) and analytical solutions for carbon and silica carbide nanotubes under C–C and C–F boundary conditions. In the present study, the C–C boundary condition is achieved by assigning the spring stiffness coefficients as $\gamma_0 = \gamma_L = 10^{14}$ nN/nm, while the C–F boundary condition is modeled by taking $\gamma_0 = 10^{14}$ nN/nm and $\gamma_L = 10^{-6}$ nN/nm. The comparisons are carried out within the framework of classical elasticity ($\mu = 0$) for different elastic foundation parameters. For the C–C boundary condition, the proposed Fourier–Stokes solution shows excellent agreement with the results of Civalek et al. [73] even with a small number of terms ($r=10$). For the C–F boundary condition, the results exhibit a convergent behavior; in particular, when the number of terms is increased to $r=150$, the relative error falls below 0.1%. These results demonstrate the accuracy, efficiency, and flexibility of the proposed method in modeling different boundary conditions.

Table 3 presents a detailed convergence analysis of the proposed solution for both C–C and C–F boundary conditions under different elastic foundation conditions and MLSPs. The closed-form expressions for solving DFs in the C–C cases ($\overline{\omega}_{C-C}$) and C–F cases ($\overline{\omega}_{C-F}$) are presented as follows:

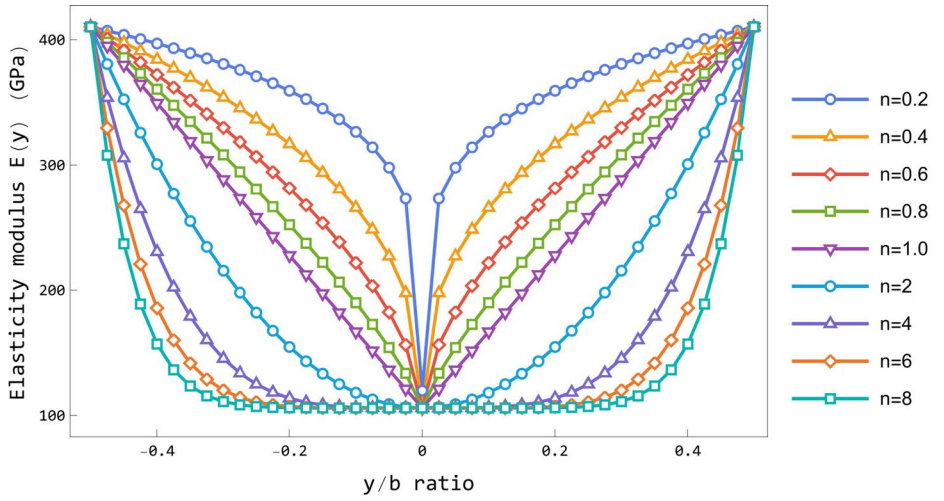
$$\overline{\omega}_{C-C} = \sqrt{\frac{k + \mu^2 A_E \left(\frac{n_m \pi}{L}\right)^4 + A_E \left(\frac{n_m \pi}{L}\right)^2}{A_\rho}} L \sqrt{\frac{\rho_c}{E_c}} \tag{59}$$

$$\overline{\omega}_{C-F} = \sqrt{\frac{k + \mu^2 A_E \left(\frac{(2n_m-1)\pi}{2L}\right)^4 + A_E \left(\frac{(2n_m-1)\pi}{2L}\right)^2}{A_\rho}} L \sqrt{\frac{\rho_c}{E_c}} \tag{60}$$

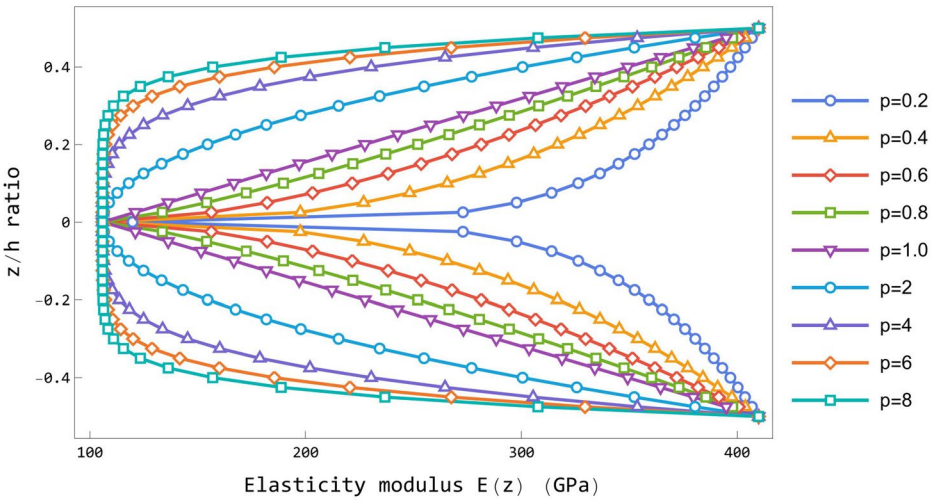
Here, n_m denotes the mode number. For the C–C case ($\gamma_0 = \gamma_L = 10^{14}$ nN/nm), the results obtained with $r=10$, 20, and 30 terms show excellent agreement with the analytical solutions, indicating that a small number of terms is sufficient to accurately capture the dynamic behavior. For the C–F boundary conditions ($\gamma_0 = 10^{14}$ nN/nm and $\gamma_L = 10^{-6}$ nN/nm), convergence is examined using $r=150$, 100, and 50 terms. The results demonstrate that the proposed solution converges to the analytical solutions with relative errors below 1%. These findings confirm that the proposed Fourier–Stokes solution can achieve excellent agreement depending on the prescribed boundary conditions, demonstrating its capability to accurately model both rigid and flexible constraints.

The variation of the elasticity modulus for different values of the material grading indices is shown in Fig. 3a–c, while Figs. 4a–c illustrate the corresponding distributions of mass density. In these figures, the effect of the material grading coefficients n and p on the material distribution in the BD-FG microbar is investigated. Figure 3a corresponds to the case where $p = 0$, indicating material variation only along the width direction (y-axis). Figure 3b represents the case where $n = 0$, reflecting variation only along the thickness direction (z-axis). Figure 3c, on the other hand, illustrates the case where $n = p$, meaning that the material properties vary in both the y- and z-directions. It should be noted that the limiting cases of the material grading indices

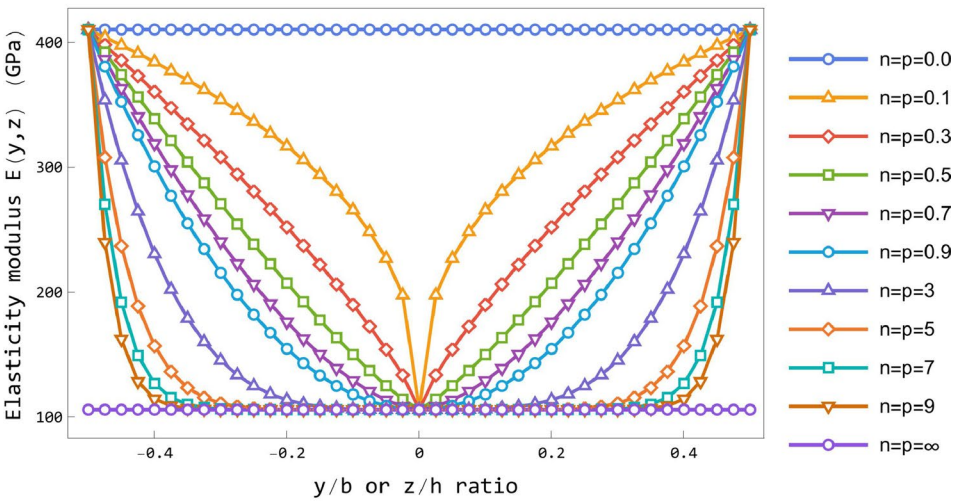
Fig. 3 Variation of the elasticity modulus $E(y, z)$ in different directions of the microbar



(a) Variation of the elasticity modulus only along the y-direction

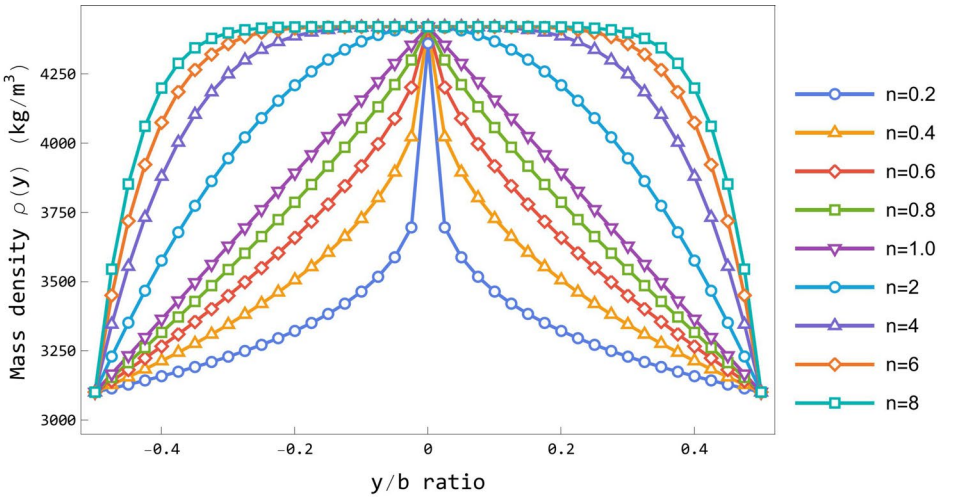


(b) Variation of the elasticity modulus only along the z-direction

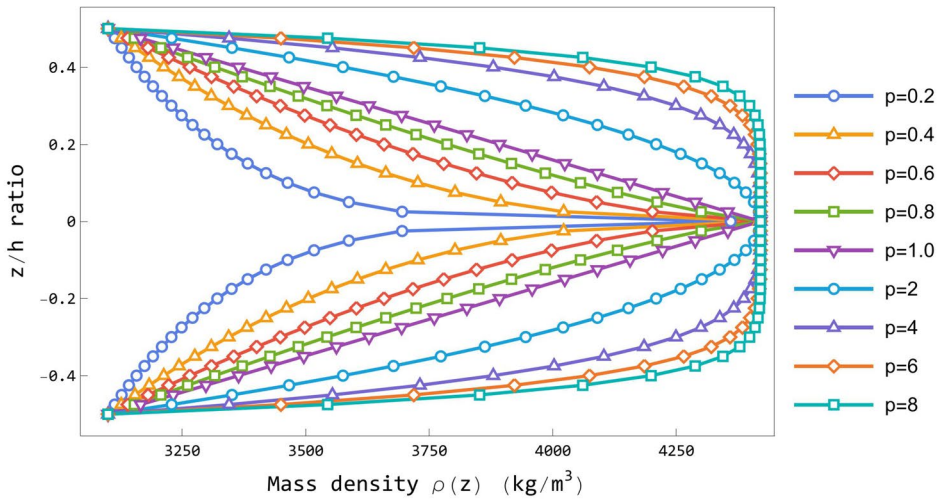


(c) Bi-directional variation of the elasticity modulus

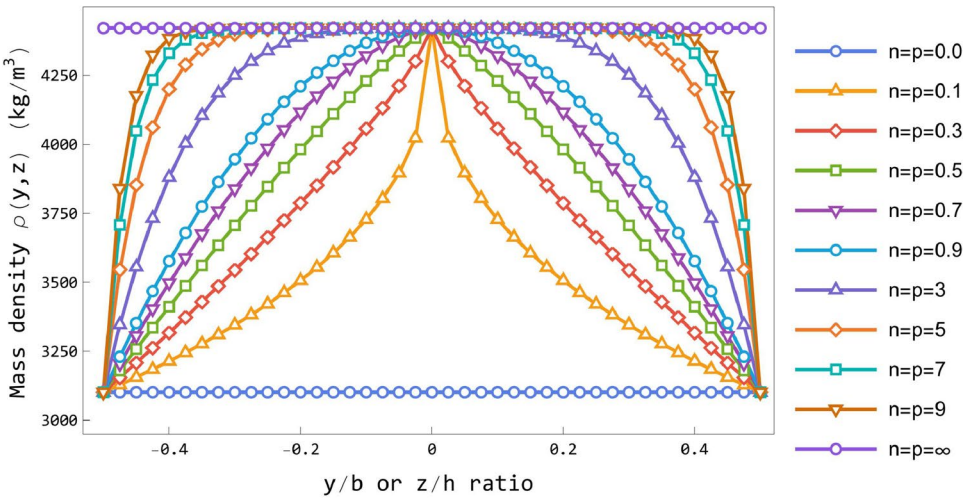
Fig. 4 Variation of the mass density $\rho(y, z)$ in different directions of the microbar



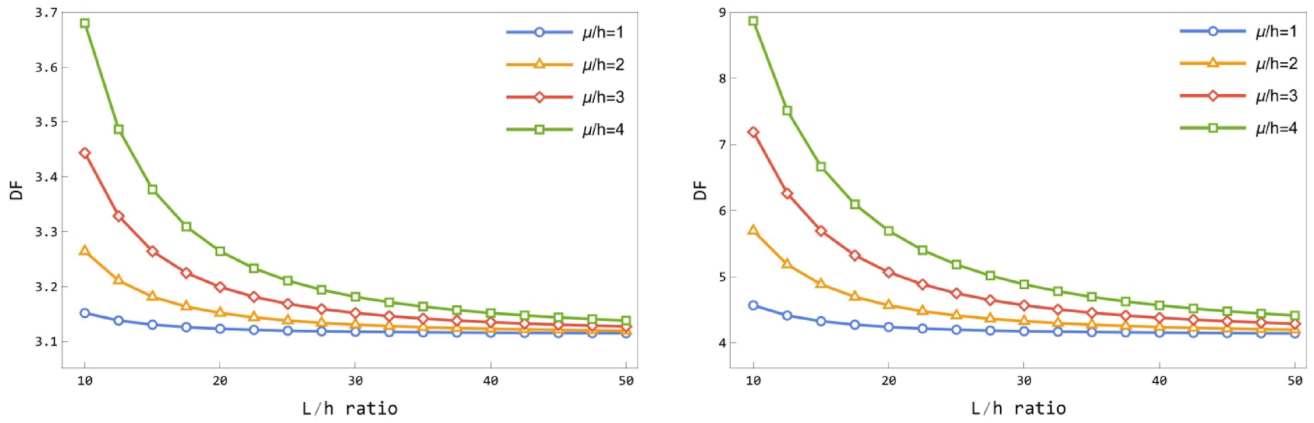
(a) Mass density variation only along the y-direction



(b) Mass density variation only along the z-direction

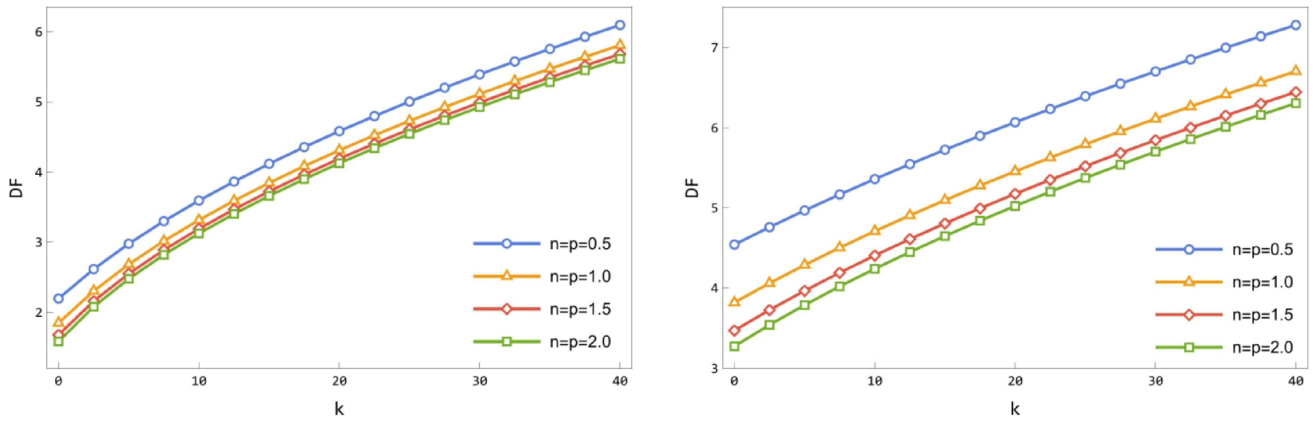


(c) Bi-directional variation of the mass density

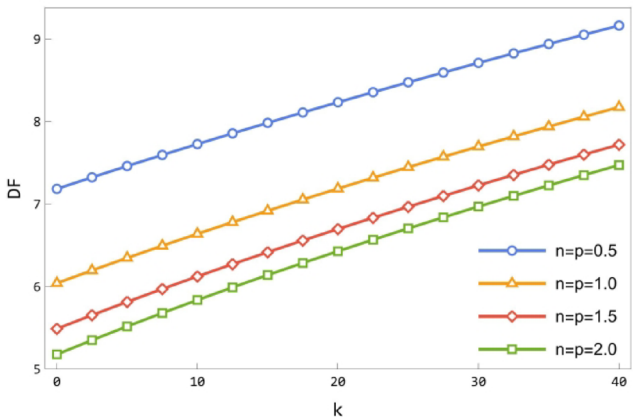


(a) Variation of DFs in the first mode (b) Variation of DFs in the second mode

Fig. 5 The influence of microbar length and MLSP on DFs



(a) First mode (b) Second mode



(c) Third mode

Fig. 6 Effect of material grading and elastic foundation on DFs in different modes

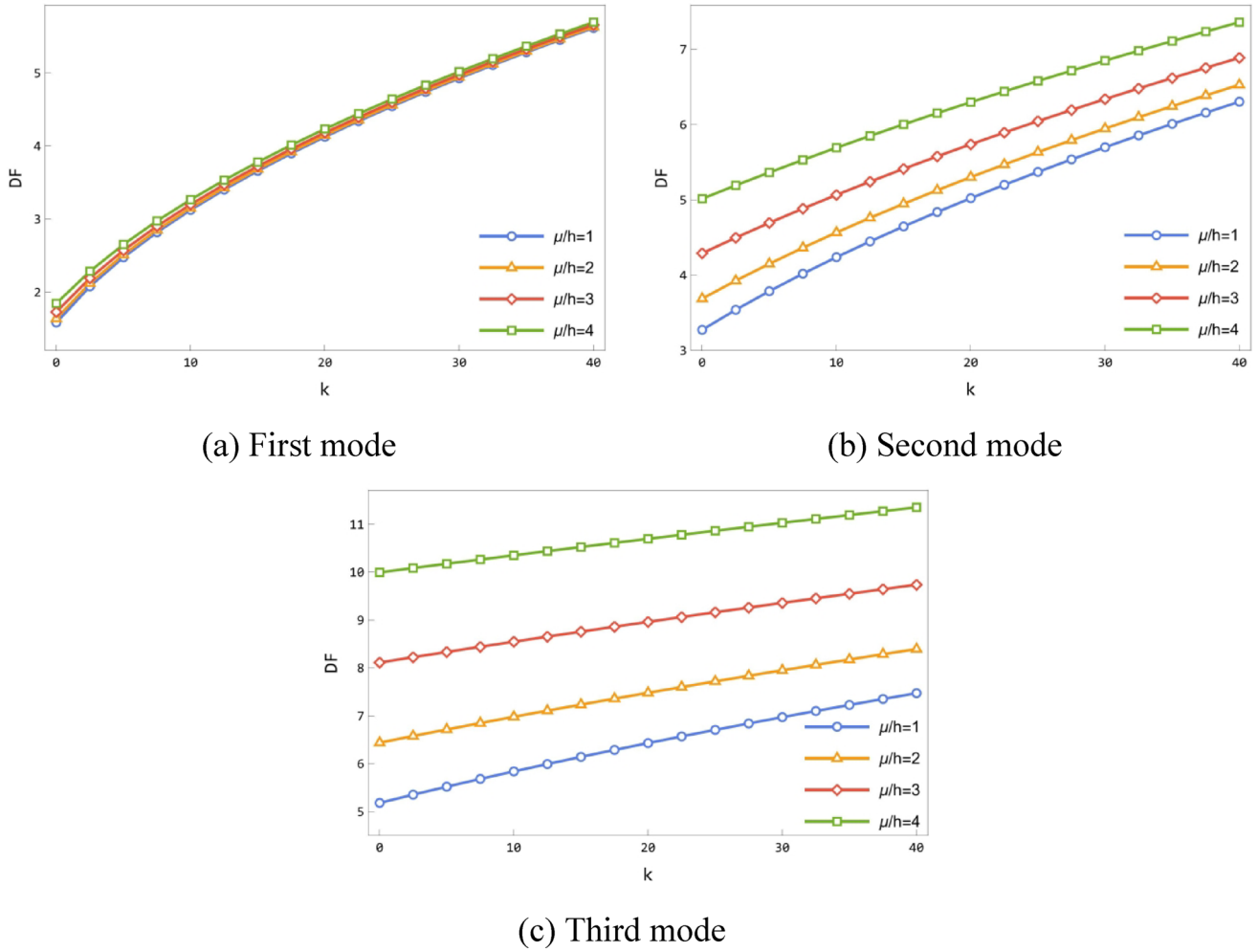


Fig. 7 Effect of MLSP and elastic foundation stiffness on DFs for different vibration modes

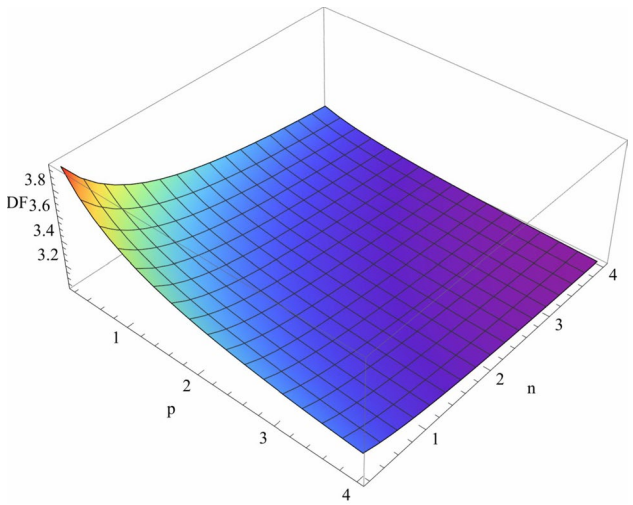


Fig. 8 Impact of varying values of material grading coefficients on DFs

are such that $n = p = 0$ corresponds to a ceramic phase, whereas $n = p = \infty$ represents a metal phase. As seen in the figures, the elastic modulus transitions from ceramic-rich to metal-rich phases depending on the values of n and p. Similarly, Fig. 4a–c demonstrate the spatial distribution of mass density under the same grading conditions. These figures highlight how increasing the material grading coefficients leads to a more metallic character, whereas lower values favor the dominance of ceramic properties in the structure.

The variation of DFs with respect to the L/h and the μ/h ratios is illustrated in Fig. 5a and 5b for the first and second modes, respectively. As observed in both figures, the DFs decrease as L/h increases. Conversely, higher μ/h values result in increased frequencies, reflecting the amplifying effect of microscale characteristics. This effect is more pronounced at lower L/h values, where size-dependent behavior becomes significant. As L/h continues to increase, the influence of μ/h becomes less significant for both modes, and the results tend to converge regardless of the MLSP. Additionally,

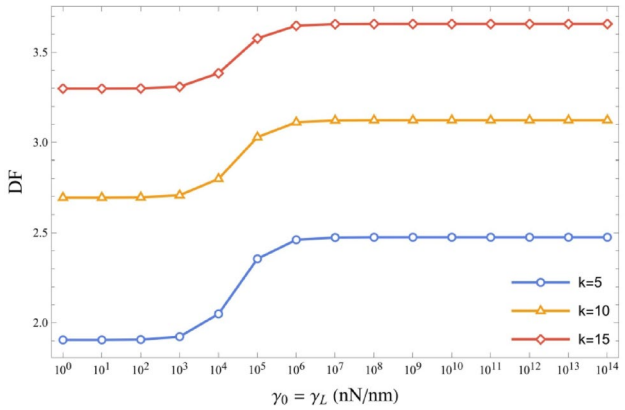


Fig. 9 Effect of boundary spring stiffnesses and elastic foundation stiffness on DFs

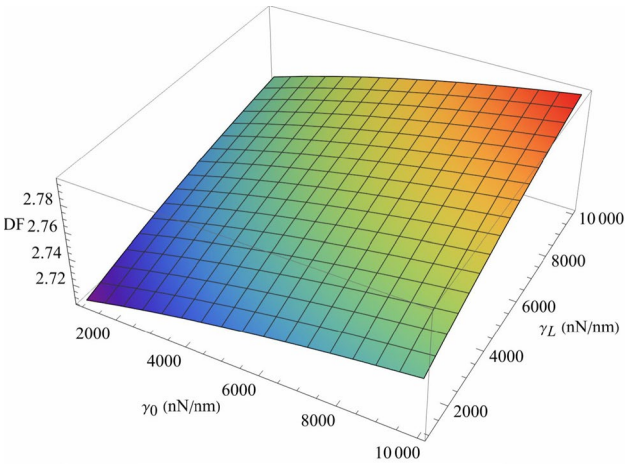


Fig. 10 Variation of DFs for different spring stiffness values

Fig. 5a and b show that the effect of μ/h on DFs is similarly significant for both the first and second modes.

Figures 6a–c show the variation of DFs with the k parameters for different values of $n = p$: (a) first mode, (b) second mode, and (c) third mode. It is observed that for all modes, the DFs increase as the elastic foundation stiffness coefficient increases, indicating the strengthening effects of the elastic foundation on the vibration frequencies. Additionally, as the parameters $n = p$ increase from 0.5 to 2, the overall frequency levels tend to decrease for each mode, mainly due to the increasing metal content relative to ceramic, which raises the effective mass and produces a softening effect on the system's dynamic response. The rate of increase in frequency with respect to the foundation coefficients is similar across all $n = p$ values. Furthermore, the influence of the material grading index on the DFs varies notably with the mode number and the elastic foundation stiffness coefficients. At higher modes, the frequency differences between varying $n = p$ values are more pronounced, indicating a higher sensitivity of fundamental vibration characteristics to material gradation. As the mode number decreases, these differences diminish, suggesting that lower vibration modes are less affected by gradation. Furthermore, increasing the elastic foundation parameter raises the frequency values for all material grading indices. However, this increase also lessens the relative differences in frequency caused by changes in the grading index. In other words, a stiffer elastic foundation reduces the effect of material gradation on the system's vibration behavior, making the frequencies more uniform.

Figure 7a–c present the variation of the DFs with elastic foundation stiffness for different MLSP values in the first, second, and third modes. In Fig. 7a, an overall increase in frequency is observed as both μ/h and k increase, though the influence of μ/h remains relatively limited at this first mode. In contrast, Fig. 7b and c show that the effect of the μ/h becomes more pronounced in the second and third modes. The frequency differences between $\mu/h = 1$ and $\mu/h = 4$ grow significantly with increasing mode number. Meanwhile, the elastic foundation parameter consistently increases the frequency values across all μ/h ratios in each mode, but it does not significantly affect the difference between the μ/h curves. Also, the effect of μ/h becomes more dominant in higher modes.

Figure 8 illustrates the variation of DFs with respect to the parameters n and p. As both n and p increase, indicating a higher metal content within the FG material, the DFs consistently decrease. This behavior is attributed to the fact that increasing the metal fraction raises the overall density while reducing the effective stiffness of the microbar, which in turn lowers the natural frequencies. Conversely, lower values of n and p, corresponding to a more ceramic-like composition, lead to higher DFs. Therefore, the results clearly demonstrate how modifying the material gradation in the BD-FG microbar significantly influences its vibration characteristics.

Figure 9 presents the variation of the DF with respect to spring stiffness for $k = 5$, $k = 10$, and $k = 15$. For all three cases, the frequency remains nearly constant at low spring stiffness values and begins to increase gradually as the stiffness exceeds a certain threshold (around 10^2–10^3 nN/nm). This behavior indicates that the influence of the spring boundary conditions becomes more significant as the springs become stiffer, approaching a clamped-like behavior. Additionally, higher k values lead to higher frequency levels across all spring stiffnesses. This occurs because a stiffer elastic foundation provides greater resistance to deformation, effectively increasing the system's overall stiffness and, consequently, its natural frequencies. These results highlight the combined effect of elastic foundation and boundary flexibility on the vibrational characteristics of the system.

Figure 10 shows the effect of varying spring stiffness at both ends of the microbar (γ_0, γ_L) on the DFs. As the spring stiffness increases, the boundary conditions approach a clamped (fixed) state, resulting in a consistent increase in the DFs. Conversely, lower spring stiffness values correspond to more flexible, free-end boundary conditions, which lead to lower DFs. For intermediate values of spring stiffness, the boundary conditions represent deformable supports. Such deformable boundaries become especially important at the micro- and nano-scale, where even small support flexibility can noticeably affect the dynamic response.

6 Conclusions

In this study, the longitudinal vibration characteristics of a BD-FG microbar resting on an elastic foundation are investigated using Aifantis SGT and deformable (spring-based) boundary conditions. The proposed formulation provides a unified framework capable of capturing size-dependent effects, material gradation, and elastic foundation interaction within a single model. Moreover, by adjusting the spring stiffness values at the boundaries, the model can reproduce different classical boundary conditions reported in the literature within the same framework. The results show excellent agreement with closed-form solutions and previously published numerical data, confirming that the proposed formulation accurately reproduces classical boundary conditions. The convergence analysis indicates that clamped boundary conditions (high spring stiffness values) are captured with very high accuracy using a small number of terms, whereas cantilever boundary conditions (one end with high and the other with low spring stiffness) are approximated with very low error as the number of terms increases. Furthermore, the numerical analyses confirm well-known trends in the axial vibration behavior of the microbar. Increasing the MLSP raises the DFs, particularly in higher modes, while increasing the microbar length reduces the frequencies and weakens size-dependent effects. Material gradation also affects the dynamic response, with higher grading indices (metal-rich configurations) leading to lower frequencies and ceramic-dominant configurations yielding higher frequencies. Additionally, increasing the stiffness of the elastic foundation and boundary springs consistently increases the DFs. Overall, the results demonstrate that the proposed model effectively captures the key factors governing the axial vibration behavior of micro-scale structures and provides a flexible and reliable tool for accurate vibration analysis and design. Future studies may focus on the inclusion of damping effects and forced vibration responses to further enhance the applicability of the proposed model in practical engineering systems.

Funding Open access funding provided by the Scientific and Technological Research Council of Türkiye (TÜBİTAK).

Data availability No data was used for the research described in the article.

Declarations

Conflict of interest The authors declare that they have no known competing financial interests or personal relationships that could have appeared to influence the work reported in this paper.

Open Access This article is licensed under a Creative Commons Attribution 4.0 International License, which permits use, sharing, adaptation, distribution and reproduction in any medium or format, as long as you give appropriate credit to the original author(s) and the source, provide a link to the Creative Commons licence, and indicate if changes were made. The images or other third party material in this article are included in the article's Creative Commons licence, unless indicated otherwise in a credit line to the material. If material is not included in the article's Creative Commons licence and your intended use is not permitted by statutory regulation or exceeds the permitted use, you will need to obtain permission directly from the copyright holder. To view a copy of this licence, visit http://creativecommons.org/licenses/by/4.0/.

References

1. Udupa G, Shrikantha Rao S, Gangadharan KV (2012) Future applications of carbon nanotube reinforced functionally graded composite materials. In: IEEE-International Conference on Advances in Engineering, Science and Management, ICAESM-2012. pp. 399–404
2. Li Y, Feng Z, Hao L, Huang L, Xin C, Wang Y, Bilotti E, Essa K, Zhang H, Li Z, Yan F, Peijs T (2020) A review on functionally graded materials and structures via additive manufacturing: from multi-scale design to versatile functional properties. Adv Mater Technol. https://doi.org/10.1002/admt.201900981
3. Rafiee M, Farahani RD, Therriault D (2020) Multi-material 3D and 4D printing: a survey. Adv Sci. https://doi.org/10.1002/advs.201902307
4. Watari F, Yokoyama A, Omori M, Hirai T, Kondo H, Uo M, Kawasaki T (2004) Biocompatibility of materials and development to functionally graded implant for bio-medical application. Compos Sci Technol 64:893–908. https://doi.org/10.1016/J.COMPSCITECH.2003.09.005
5. Parthasarathy J, Starly B, Raman S (2011) A design for the additive manufacture of functionally graded porous structures with tailored mechanical properties for biomedical applications. J Manuf Process. https://doi.org/10.1016/j.jmapro.2011.01.004
6. Takagi K, Li JF, Yokoyama S, Watanabe R (2003) Fabrication and evaluation of PZT/Pt piezoelectric composites and functionally graded actuators. J Eur Ceram Soc 23:1577–1583. https://doi.org/10.1016/S0955-2219(02)00407-7
7. Torelli G, Fernández MG, Lees JM (2020) Functionally graded concrete: design objectives, production techniques and analysis methods for layered and continuously graded elements. Constr Build Mater 242:118040. https://doi.org/10.1016/J.CONBUILDMAT.2020.118040
8. Ahmed ZY, Bos FP, van Brunschot MCAJ, Salet TAM (2020) On-demand additive manufacturing of functionally graded concrete. Virtual Phys Prototyp. https://doi.org/10.1080/17452759.2019.1709009

9. Liu X, Yan M, Galobardes I, Sikora K (2018) Assessing the potential of functionally graded concrete using fibre reinforced and recycled aggregate concrete. Constr Build Mater 171:793–801. https://doi.org/10.1016/j.conbuildmat.2018.03.202
10. Müller E, Drašar Č, Schilz J, Kaysser WA (2003) Functionally graded materials for sensor and energy applications. Mater Sci Eng A 362:17–39. https://doi.org/10.1016/S0921-5093(03)00581-1
11. Aifantis EC (1999) Strain gradient interpretation of size effects. Int J Fract 95:299–314. https://doi.org/10.1007/978-94-011-4659-3_16
12. Aifantis EC (1992) On the role of gradients in the localization of deformation and fracture. Int J Eng Sci 30:1279–1299. https://doi.org/10.1016/0020-7225(92)90141-3
13. Lim CW, Zhang G, Reddy JN (2015) A higher-order nonlocal elasticity and strain gradient theory and its applications in wave propagation. J Mech Phys Solids 78:298–313. https://doi.org/10.1016/j.jmps.2015.02.001
14. Lam DCC, Yang F, Chong ACM, Wang J, Tong P (2003) Experiments and theory in strain gradient elasticity. J Mech Phys Solids 51:1477–1508. https://doi.org/10.1016/S0022-5096(03)00053-X
15. Bahrami A, Zargaripoor A, Khojastehnezhad VM, Pourasl HH (2024) Size-dependent free vibration of functionally graded beams with a tip nanoparticle and a nonlinear spring constraint via strain gradient theory. Mech Adv Mater Struct 31:1746–1759. https://doi.org/10.1080/15376494.2022.2141386
16. Zanoosi AAP (2020) Size-dependent thermo-mechanical free vibration analysis of functionally graded porous microbeams based on modified strain gradient theory. J Braz Soc Mech Sci Eng 42:236. https://doi.org/10.1007/s40430-020-02340-3
17. Wang L (2012) Vibration analysis of nanotubes conveying fluid based on gradient elasticity theory. J Vib Control 18:313–320. https://doi.org/10.1177/1077546311403957
18. Rouhi H, Ebrahimi F, Ansari R, Torabi J (2019) Nonlinear free and forced vibration analysis of Timoshenko nanobeams based on Mindlin's second strain gradient theory. Eur J Mech A Solids 73:268–281. https://doi.org/10.1016/j.euromechsol.2018.09.005
19. Jiang J, Wang L (2018) Analytical solutions for the thermal vibration of strain gradient beams with elastic boundary conditions. Acta Mech 229:2203–2219. https://doi.org/10.1007/s00707-017-2105-z
20. Ansari R, Gholami R, Rouhi H (2012) Vibration analysis of single-walled carbon nanotubes using different gradient elasticity theories. Compos B Eng 43:2985–2989. https://doi.org/10.1016/j.compositesb.2012.05.049
21. Wang L, He X, Sun Y, Liew KM (2017) A mesh-free vibration analysis of strain gradient nano-beams. Eng Anal Bound Elem 84:231–236. https://doi.org/10.1016/j.enganabound.2017.09.001
22. Shahriari B, Karamooz Ravari MR, Zeighampour H (2015) Vibration analysis of functionally graded carbon nanotube-reinforced composite nanoplates using Mindlin's strain gradient theory. Compos Struct 134:1036–1043. https://doi.org/10.1016/j.compstruct.2015.08.118
23. Uzun B (2025) An innovative analytical simulation for scale-dependent transverse vibration of isolated protein microtubules. J Braz Soc Mech Sci Eng , 47:359. https://doi.org/10.1007/s40430-025-05644-4
24. Akgöz B, Civalek Ö (2013) Buckling analysis of functionally graded microbeams based on the strain gradient theory. Acta Mech 224:2185–2201. https://doi.org/10.1007/s00707-013-0883-5
25. Mohammadi H, Mahzoon M (2014) Investigating thermal effects in nonlinear buckling analysis of micro beams using modified strain gradient theory. Iran J Sci Technol - Trans Mech Eng 38:303–320
26. Arda M (2020) Buckling analysis of intermediately supported nanobeams via strain gradient elasticity theory. Int J Eng Appl Sci 12:163–172. https://doi.org/10.24107/ijeas.842499
27. Yayli MÖ (2011) Stability analysis of a gradient elastic beam using finite element method. Int J Phys Sci 6:2844–2851. https://doi.org/10.5897/IJPS11.361
28. Yaylı MÖ (2015) Stability analysis of gradient elastic microbeams with arbitrary boundary conditions. J Mech Sci Technol 29:3373–3380. https://doi.org/10.1007/s12206-015-0735-4
29. Akgöz B, Civalek Ö (2016) Bending analysis of embedded carbon nanotubes resting on an elastic foundation using strain gradient theory. Acta Astronaut 119:1–12. https://doi.org/10.1016/J.ACTAASTRO.2015.10.021
30. Akgöz B, Civalek Ö (2012) Analysis of micro-sized beams for various boundary conditions based on the strain gradient elasticity theory. Arch Appl Mech 82:423–443. https://doi.org/10.1007/s00419-011-0565-5
31. Gholami M, Alizadeh M (2022) A quasi-3D modified strain gradient formulation for static bending of functionally graded micro beams resting on Winkler-Pasternak elastic foundation. Sci Iran 29:26–40. https://doi.org/10.24200/sci.2021.55000.4019
32. Akgöz B, Civalek Ö (2015) Bending analysis of FG microbeams resting on Winkler elastic foundation via strain gradient elasticity. Compos Struct 134:294–301. https://doi.org/10.1016/J.COMPSTRUCT.2015.08.095
33. Akgöz B, Civalek Ö (2022) Buckling Analysis of Functionally Graded Tapered Microbeams via Rayleigh-Ritz Method. Mathematics 10:4429. https://doi.org/10.3390/math10234429
34. Li YS, Feng WJ, Cai ZY (2014) Bending and free vibration of functionally graded piezoelectric beam based on modified strain gradient theory. Compos Struct 115:41–50. https://doi.org/10.1016/j.compstruct.2014.04.005
35. Chu L, Dui G, Ju C (2018) Flexoelectric effect on the bending and vibration responses of functionally graded piezoelectric nanobeams based on general modified strain gradient theory. Compos Struct 186:39–49. https://doi.org/10.1016/j.compstruct.2017.10.083
36. Lei J, He Y, Zhang B, Gan Z, Zeng P (2013) Bending and vibration of functionally graded sinusoidal microbeams based on the strain gradient elasticity theory. Int J Eng Sci 72:36–52. https://doi.org/10.1016/j.ijengsci.2013.06.012
37. Wang YQ, Zhao HL, Ye C, Zu JW (2018) A porous microbeam model for bending and vibration analysis based on the sinusoidal beam theory and modified strain gradient theory. Int J Appl Mech. https://doi.org/10.1142/S175882511850059X
38. Wang B, Zhao J, Zhou S (2010) A micro scale Timoshenko beam model based on strain gradient elasticity theory. Eur J Mech A/Solids 29:591–599. https://doi.org/10.1016/j.euromechsol.2009.12.005
39. Ansari R, Gholami R, Faghih Shojaei M, Mohammadi V, Sahmani S (2013) Size-dependent bending, buckling and free vibration of functionally graded Timoshenko microbeams based on the most general strain gradient theory. Compos Struct 100:385–397. https://doi.org/10.1016/j.compstruct.2012.12.048
40. Zhao X, Zheng S, Li Z (2022) Bending, free vibration and buckling analyses of AFG flexoelectric nanobeams based on the strain gradient theory. Mech Adv Mater Struct 29:548–563. https://doi.org/10.1080/15376494.2020.1779880
41. Nguyen ND, Bui VT, Nguyen TK (2024) A modified strain gradient theory for buckling, bending and free vibration behaviors of metal foam microbeams. Structures 64:106533. https://doi.org/10.1016/j.istruc.2024.106533
42. Karamanli A, Vo TP (2020) Size-dependent behaviour of functionally graded sandwich microbeams based on the modified strain gradient theory. Compos Struct 246:112401. https://doi.org/10.1016/j.compstruct.2020.112401
43. Zhang B, He Y, Liu D, Gan Z, Shen L (2014) Non-classical Timoshenko beam element based on the strain gradient elasticity

theory. Finite Elem Anal Des 79:22–39. https://doi.org/10.1016/j.finel.2013.10.004
44. Zhao J, Zhou S, Wang B, Wang X (2012) Nonlinear microbeam model based on strain gradient theory. Appl Math Model 36:2674–2686. https://doi.org/10.1016/j.apm.2011.09.051
45. Barretta R, Faghidian SA, Marotti de Sciarra F, Penna R, Pinnola FP (2020) On torsion of nonlocal Lam strain gradient FG elastic beams. Compos Struct 233:111550. https://doi.org/10.1016/j.compstruct.2019.111550
46. Kafkas U, Uzun B, Yaylı MÖ (2024) Analyzing torsional vibration in restrained functionally graded nanobeams: nonlocal Lam strain gradient approach. J Braz Soc Mech Sci Eng 46:1–19. https://doi.org/10.1007/s40430-024-05059-7
47. Akpınar M, Kafkas U, Uzun B, Yaylı MÖ (2025) On the torsional vibration of a porous nanorod with arbitrary boundary conditions considering nonlocal lam strain gradient theory. Eur J Mech A Solids 111:105610. https://doi.org/10.1016/j.euromechsol.2025.105610
48. Noroozi R, Barati A, Kazemi A, Norouzi S, Hadi A (2020) Torsional vibration analysis of bi-directional FG nano-cone with arbitrary cross-section based on nonlocal strain gradient elasticity. Adv Nano Res 8:13–24. https://doi.org/10.12989/ANR.2020.8.1.013
49. Guo S, He Y, Liu D, Lei J, Shen L, Li Z (2016) Torsional vibration of carbon nanotube with axial velocity and velocity gradient effect. Int J Mech Sci 119:88–96. https://doi.org/10.1016/j.ijmecsci.2016.09.036
50. Uzun B, Yaylı MÖ, Civalek Ö (2024) An investigation on the torsional vibration of a FG strain gradient nanotube. ZAMM J Appl Math Mech 104:e202301093. https://doi.org/10.1002/ZAMM.202301093
51. Narendar S, Ravinder S, Gopalakrishnan S (2012) Strain gradient torsional vibration analysis of micro / nano rods. Int J Nano Dimens 3:1–17
52. Adeli MM, Hadi A, Hosseini M, Gorgani HH (2017) Torsional vibration of nano-cone based on nonlocal strain gradient elasticity theory. Eur Phys J Plus 132:1–10. https://doi.org/10.1140/epjp/i2017-11688-0
53. Hamidi BA, Hosseini SA, Hayati H (2022) Forced torsional vibration of nanobeam via nonlocal strain gradient theory and surface energy effects under moving harmonic torque. Waves Random Complex Media 32:318–333. https://doi.org/10.1080/17455030.2020.1772523
54. Kahrobaiyan MH, Tajalli SA, Movahhedy MR, Akbari J, Ahmadian MT (2011) Torsion of strain gradient bars. Int J Eng Sci 49:856–866. https://doi.org/10.1016/j.ijengsci.2011.04.008
55. Ansari R, Gholami R, Ajori S (2013) Torsional vibration analysis of carbon nanotubes based on the strain gradient theory and molecular dynamic simulations. J Vib Acoust. https://doi.org/10.1115/1.4024208/380056
56. El-Borgi S, Rajendran P, Friswell MI, Trabelssi M, Reddy JN (2018) Torsional vibration of size-dependent viscoelastic rods using nonlocal strain and velocity gradient theory. Compos Struct 186:274–292. https://doi.org/10.1016/j.compstruct.2017.12.002
57. Altan BS, Evensen HA, Aifantis EC (1996) Longitudinal vibrations of a beam: a gradient elasticity approach. Mech Res Commun 23:35–40. https://doi.org/10.1016/0093-6413(95)00074-7
58. Kahrobaiyan MH, Asghari M, Ahmadian MT (2013) Longitudinal behavior of strain gradient bars. Int J Eng Sci 66–67:44–59. https://doi.org/10.1016/j.ijengsci.2013.02.005
59. Akgöz B, Civalek Ö (2014) Longitudinal vibration analysis for microbars based on strain gradient elasticity theory. J Vib Control 20:606–616. https://doi.org/10.1177/1077546312463752
60. Akgöz B, Civalek Ö (2013) Longitudinal vibration analysis of strain gradient bars made of functionally graded materials (FGM). Compos Part B Eng 55:263–268. https://doi.org/10.1016/j.compositesb.2013.06.035
61. Dimosthenis V (2024) Longitudinal vibration analysis of strain gradient elastic bar with various boundary conditions. J Appl Eng Sci 22:665–680. https://doi.org/10.5937/jaes0-51432
62. Şimşek M (2016) Axial vibration analysis of a nanorod embedded in elastic medium using nonlocal strain gradient theory. Cukurova Univ J Fac Eng Archit 31:213–221
63. Li L, Hu Y, Li X (2016) Longitudinal vibration of size-dependent rods via nonlocal strain gradient theory. Int J Mech Sci 115–116:135–144. https://doi.org/10.1016/J.IJMECSCI.2016.06.011
64. Gul U, Aydogdu M (2022) Longitudinal vibration of Bishop nanorods model based on nonlocal strain gradient theory. J Braz Soc Mech Sci Eng 44:1–14. https://doi.org/10.1007/s40430-022-03635-3
65. Uzun B, Civalek Ö, Yaylı MÖ (2022) Axial and torsional free vibrations of restrained single-walled boron nitride nanotube (SWBNNT) embedded in an elastic medium via nonlocal strain gradient theory. Waves Random Complex Media. https://doi.org/10.1080/17455030.2022.2147600
66. Jin H, Sui S, Zhu C, Li C (2023) Axial free vibration of rotating FG piezoelectric nano-rods accounting for nonlocal and strain gradient effects. J Vib Eng Technol 11:537–549. https://doi.org/10.1007/s42417-022-00592-y
67. Balci MN (2022) Longitudinal vibration of a nanorod embedded in viscoelastic medium considering nonlocal strain gradient theory. Adv Nano Res 13:147–164. https://doi.org/10.12989/anr.2022.13.2.147
68. Zhu X, Li L (2017) On longitudinal dynamics of nanorods. Int J Eng Sci 120:129–145. https://doi.org/10.1016/j.ijengsci.2017.08.003
69. Shatalov M, Marais J, Fedotov I, Djouosseu M (2011) longitudinal vibration of ısotropic solid rods: from classical to modern theories. In: Advances in computer science and engineering. InTech
70. Barretta R, Faghidian SA, Luciano R (2019) Longitudinal vibrations of nano-rods by stress-driven integral elasticity. Mech Adv Mater Struct 26:1307–1315. https://doi.org/10.1080/15376494.2018.1432806
71. Hamidi BA, Hosseini SA, Hayati H, Hassannejad R (2022) Forced axial vibration of micro and nanobeam under axial harmonic moving and constant distributed forces via nonlocal strain gradient theory. Mech Based Des Struct Mach 50:1491–1505. https://doi.org/10.1080/15397734.2020.1744003
72. Uzun B, Civalek Ö, Yaylı MÖ (2022) Nonlocal strain gradient approach for axial vibration analysis of arbitrary restrained nanorod. J Braz Soc Mech Sci Eng 44:532. https://doi.org/10.1007/s40430-022-03823-1
73. Civalek Ö, Uzun B, Yaylı MÖ, Akgöz B (2020) Size-dependent transverse and longitudinal vibrations of embedded carbon and silica carbide nanotubes by nonlocal finite element method. Eur Phys J Plus 135:381. https://doi.org/10.1140/epjp/s13360-020-00385-w
74. Nassef ASE (2026) Variable cross section nanorod model for longitudinal vibration analysis of cracked nanorods. Mater Today Commun 50:114305. https://doi.org/10.1016/j.mtcomm.2025.114305
75. Akpınar M, Kafkas U, Uzun B, Yaylı MÖ (2025) Size-dependent longitudinal vibration of embedded FG Bishop nanotubes by incorporating deformable boundary conditions. Int J Mech Mater Des. https://doi.org/10.1007/s10999-025-09778-0
76. Balci MN (2025) Axial forced vibration problem for a viscoelastic nanorod involving radially graded porosity. J Braz Soc Mech Sci Eng 47:203-. https://doi.org/10.1007/s40430-025-05497-x
77. Bouzidi I, Hadjoui A, Fellah A (2021) Dynamic analysis of functionally graded rotor-blade system using the classical version of the finite element method. Mech Based Des Struct Mach 49:1080–1108. https://doi.org/10.1080/15397734.2019.1706558

78. Hassaine N, Touat N, Dahak M, Fellah A, Saimi A (2024) Study of crack's effect on the natural frequencies of bi-directional functionally graded beam. Mech Based Des Struct Mach 52:375–385. https://doi.org/10.1080/15397734.2022.2113408
79. Akgöz B, Civalek Ö (2013) Free vibration analysis of axially functionally graded tapered Bernoulli-Euler microbeams based on the modified couple stress theory. Compos Struct 98:314–322. https://doi.org/10.1016/j.compstruct.2012.11.020
80. Askes H, Aifantis EC (2011) Gradient elasticity in statics and dynamics: An overview of formulations, length scale identification procedures, finite element implementations and new results. Int J Solids Struct 48:1962–1990. https://doi.org/10.1016/j.ijsolstr.2011.03.006
81. Reddy JN, Kim J (2012) A nonlinear modified couple stress-based third-order theory of functionally graded plates. Compos Struct 94:1128–1143. https://doi.org/10.1016/j.compstruct.2011.10.006
82. Ghayesh MH, Farokhi H, Amabili M (2013) Nonlinear dynamics of a microscale beam based on the modified couple stress theory. Compos Part B Eng 50:318–324. https://doi.org/10.1016/j.compositesb.2013.02.021
83. Vel SS (2010) Exact elasticity solution for the vibration of functionally graded anisotropic cylindrical shells. Compos Struct 92:2712–2727. https://doi.org/10.1016/j.compstruct.2010.03.012

Publisher's Note Springer Nature remains neutral with regard to jurisdictional claims in published maps and institutional affiliations.